Journal of
Synchrotron
Radiation

ISSN 1600-5775

Received 12 April 2014
Accepted 22 September 2014

In situ synchrotron X-ray diffraction analysis of deformation behaviour in Ti–Ni-based thin films

Hong Wang,[a] Guangai Sun,[a,b]* Xiaolin Wang,[a] Bo Chen,[a] Xiaotao Zu,[c] Yanping Liu,[b,d] Liangbin Li,[b,d] Guoqiang Pan,[d] Liusi Sheng,[b] Yaoguang Liu[a] and Yong Qing Fu[e]*

[a]Institute of Nuclear Physics and Chemistry, Mianyang 621900, People's Republic of China, [b]College of Nuclear Science and Technology, University of Science and Technology of China, Hefei 230029, People's Republic of China, [c]Department of Applied Physics, University of Electronic Science and Technology of China, Chengdu 610054, People's Republic of China, [d]National Synchrotron Radiation Laboratory, University of Science and Technology of China, Hefei 230029, People's Republic of China, and [e]Thin Film Centre, Scottish Universities of Physics Alliance (SUPA), University of the West of Scotland, Paisley PA1 2BE, UK. *E-mail: guangaisun80@gmail.com, richard.fu@uws.ac.uk

Deformation mechanisms of as-deposited and post-annealed $Ti_{50.2}Ni_{49.6}$, $Ti_{50.3}Ni_{46.2}Cu_{3.5}$ and $Ti_{48.5}Ni_{40.8}Cu_{7.5}$ thin films were investigated using the *in situ* synchrotron X-ray diffraction technique. Results showed that initial crystalline phases determined the deformation mechanisms of all the films during tensile loading. For the films dominated by monoclinic martensites (B19′), tensile stress induced the detwinning of ⟨011⟩ type-II twins and resulted in the preferred orientations of $(002)_{B19'}$ parallel to the loading direction (∥ LD) and $(020)_{B19'}$ perpendicular to the LD (⊥ LD). For the films dominated by austenite (B2), the austenite directly transformed into martensitic variants (B19′) with preferred orientations of $(002)_{B19'}$ ∥ LD and $(020)_{B19'}$ ⊥ LD. For the $Ti_{50.3}Ni_{46.2}Cu_{3.5}$ and $Ti_{48.1}Ni_{40.8}Cu_{7.5}$ films, martensitic transformation temperatures decreased apparently after post-annealing because of the large thermal stress generated in the films due to the large differences in thermal expansion coefficients between the film and substrate.

Keywords: shape memory; Ti–Ni; thin film; deformation behaviour; detwinning; synchrotron X-ray diffraction.

1. Introduction

Ti–Ni-based shape memory alloys (SMAs) have been extensively investigated in the past three decades due to their excellent properties, including shape memory effect, superelasticity and biocompatibility (Miyazaki & Ishida, 1999; Fu *et al.*, 2001, 2004; Miyazaki *et al.*, 2009; Sun *et al.*, 2012). Substitution of Cu for Ni in the Ti–Ni SMAs has been well known to reduce the composition sensitivity to martensitic transformation temperatures, narrow the transformation hysteresis, and change the transformation temperatures (Otsuka & Ren, 2005). Recently there have been extensive studies using the sputter-deposited Ti–Ni and Ti–Ni–Cu thin films to make microactuators and microelectromechanical system (MEMS) components (Miyazaki & Ishida, 1999; Fu *et al.*, 2004). In order to make high-performance micro-actuators using the Ti–Ni-based films, a systematic study of their deformation mechanism is crucial.

Previous investigations (Miyazaki & Ishida, 1999; Fu *et al.*, 2001; Chu *et al.*, 2000; Du & Fu, 2004; Zhang & Qiu, 2006; Ishida *et al.*, 2013) have been focusing on the deposition, microstructure and thermomechanical characterization of these thin films, and various methods have been used to study the stress-induced phase transformation of the Ti–Ni-based SMA films, such as tensile tests (Ishida *et al.*, 1996), dynamic mechanical-thermo analysis (DMTA) (Zarnetta *et al.*, 2009) and transmission electron microscopy (TEM) (Zhang *et al.*, 2006; Ishida *et al.*, 2008; Meng *et al.*, 2008*a*,*b*, 2009, 2011). Compared with the above *ex situ* methods, *in situ* diffraction characterization techniques during thermomechanical loading are capable of providing *in situ* analysis of microstructure evolution, exactly corresponding to the stress-induced phase transformation processes (Malard *et al.*, 2012). Among these *in situ* diffraction techniques, the *in situ* synchrotron X-ray diffraction (S-XRD) method has been used as a powerful tool to study the stress-induced phase transformation of the bulk

Table 1
Film deposition parameters and characterization properties.

Film composition (at.%)	Target power (W)			Post-annealing temperature (°C)	Transformation temperature (°C)				Film thickness (μm)
	Ti–Ni (RF)	Ti (DC)	Cu (DC)		M_s (R_s)	M_f (R_f)	A_s	A_f	
Ti–Ni ($Ti_{50.2}Ni_{49.6}$)	$Ti_{50}Ni_{50}$ 400	70	0	As-deposited	38 (63)	19.4 (58)	73	84	4.5
				650	64	40	74	100	
				750	64.5	53.2	80.2	95.4	
Ti–Ni–Cu 3.5 ($Ti_{50.3}Ni_{46.2}Cu_{3.5}$)	$Ti_{55}Ni_{45}$ 400	0	2.5	As-deposited	50	38	65	75.3	4.5
				650	22	0	25.8	36.2	
				750	23.4	16.1	40	55.7	
Ti–Ni–Cu 7.5 ($Ti_{48.5}Ni_{40.8}Cu_{7.5}$)	$Ti_{60}Ni_{40}$ 400	0	7	As-deposited	58	34	65	75	3.5
				650	20	0	27	43	
				750	21	11	14	54	

SMAs (Kulkov *et al.*, 2000; Wang *et al.*, 2007). However, little work has been done for *in situ* S-XRD testing of the deformation behaviour of thin-film SMAs, mostly due to the difficulties in microscale testing of the free-standing films (Miyazaki & Ishida, 1999; Wang *et al.*, 2012).

For the Ti–Ni–Cu films with Cu > 10 at.%, little work has been reported on their *in situ* deformation behaviour, although TEM has been applied to *ex situ* investigate their deformation behaviours (Ishida *et al.*, 2008; Meng *et al.*, 2008*a*,*b*, 2009, 2011). In our previous reported work (Wang *et al.*, 2012), *in situ* S-XRD has been used to investigate the stress-induced phase transformation behaviour of a $Ti_{50.1}Ni_{40.8}Cu_{9.1}$ film. Results showed that the deformation mechanism of the $Ti_{50.1}Ni_{40.8}Cu_{9.1}$ film is significantly dependent on the film composition, microstructure and initial phase state (Wang *et al.*, 2012). In this paper the deformation mechanisms of various Ti–Ni and Ti–Ni–Cu films (Cu < 9 at.%) will be systematically studied using the *in situ* S-XRD method, and effects of the film composition, microstructure and post-annealing condition on the deformation mechanisms will be discussed.

2. Experimental

Thin films of Ti–Ni and Ti–Ni–Cu with three different compositions were deposited onto four-inch silicon (100) wafers by co-sputtering of Ti–Ni, Ti and Cu targets using a DC/RF magnetron sputter (Coaxial MSS3A, UK) with a base vacuum of 5×10^{-7} mTorr, which was achieved by pre-sputtering of Ti film and then pre-heating the chamber at 450°C for half an hour before loading the Si wafers. The substrate temperature during the deposition was 450°C. The composition was determined by wavelength-dispersive X-ray microanalysis (WDX) using standard samples of pure Ti and Ni (purity, 99.99%). The X-ray diffraction (XRD) measurements of the Ti–Ni and Ti–Ni–Cu films were carried out using a Philips PW3719 X-ray diffractometer. The Ti–Ni and Ti–Ni–Cu thin films on the Si substrate were post-annealed at 650 and 750°C for one hour in a vacuum furnace (ULVAC, Vacuum Annealing Furnace VHA-1015), with a based vacuum of 3×10^{-5} Torr. The deposition and post-annealing parameters of the films as well as their composition are listed in Table 1. The transformation temperatures listed in Table 1 were determined using a differential scanning calorimeter (DSC; SETARAM instrument 131) with a heating/cooling rate of 5°C min^{-1}. The following notation for the transformation temperatures was used in this paper: A_s, A_f, R_s, R_f, M_s, M_f, in which A: austenite (B2); R: martensite (R-phase); M: martensite (B19′); subscript s: starting temperature; subscript f: finishing temperature. After annealing, the free-standing films were peeled off from the Si wafer for tensile testing.

The experimental set-up for the *in situ* S-XRD measurements was previously reported by Wang *et al.* (2012), and the configurations and samples dimension are shown in Fig. 1. A miniature mechanical tester was used for the tensile test. The uniaxial loading experiments at room temperature (RT) were performed with the strains increased stepwise from 0.2% to 1.3% along the specimen's longitudinal direction, with a strain rate of 1.165 μm s^{-1}. The strain was determined using the movement of the crosshead of the mechanical testing machine, and the mechanical error of the apparatus was less than 0.02 mm with a stretching range of 100 mm. The error of the force sensor was less than 1 N. The loading direction (LD) was parallel to the direction of 0° azimuth angle (φ) in the diffraction pattern. According to Bragg's law, the data at φ = 0° correspond to crystal planes whose normals are parallel to the loading direction [*i.e.* (*hkl*) ∥ LD], and those at φ = 90° are contributed by the crystal planes whose normals are perpendicular to the loading direction [*i.e.* (*hkl*) ⊥ LD]. The *in situ* S-XRD measurements during tensile tests were performed

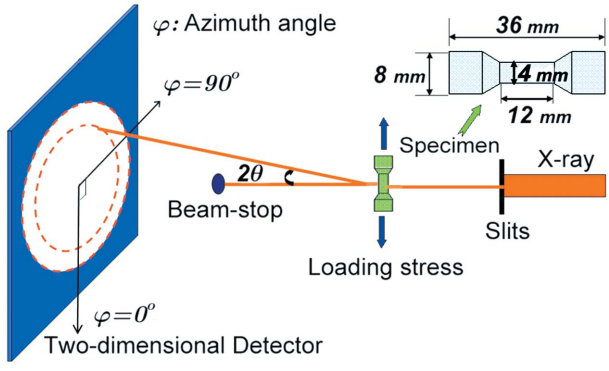

Figure 1
Experimental set-up for *in situ* S-XRD measurements and dimensions of the tensile specimen (Wang *et al.*, 2012).

at room temperature at the synchrotron radiation X-ray scattering station at the National Synchrotron Radiation Laboratory in Hefei, China. A monochromatic beam of hard X rays (λ = 0.13 nm) was used with a beam size of 4 mm × 0.5 mm. The incident direction of X-rays is perpendicular to the LD of the specimen. The measurements were performed using a transmission geometry. A two-dimensional image-plate detector was used to measure the diffracted X-rays. The software package *Fit2D* (Hammersley *et al.*, 1996) was used to analyze the two-dimensional diffraction patterns, and then the total intensity was obtained parallel or perpendicular to the loading direction.

3. Results and analysis

3.1. Microstructure evolution after post-annealing

Fig. 2 compares the room-temperature XRD results of the as-deposited Ti–Ni and Ti–Ni–Cu films, and martensites are dominant in these films. For the Ti–Ni film, both the DSC and XRD results show that the transformation from R phase to B19′ phase has not finished at room temperature, thus the microstructure is a mixture of R phase and B19′ phase at room temperature, as shown in Fig. 2. For the Ti–Ni–Cu 3.5 film, only the B19′ phase is obtained at room temperature. For the Ti–Ni–Cu 7.5 film, both B19 phase and B19′ phase are observed. These are consistent with the results from the DSC measurement as listed in Table 1.

Fig. 3 shows typical TEM microstructures obtained from the Ti–Ni film. It shows a bright-field image of the as-deposited Ti–Ni thin film at room temperature, in which large twinned B19′ monoclinic martensite plates dominate. The martensite domains have fine striations in the Ti–Ni matrix. The diffraction patterns indicate that most of the martensites are ⟨011⟩ type-II twin plates. The grain size is about 0.5 µm from the TEM analysis.

In Fig. 4, fine striations of ⟨011⟩ type-II twins are also observed in the as-deposited Ti–Ni–Cu 3.5 film. The twin widths vary from 0.01 to 0.1 µm, and the grain sizes are about 0.2–0.5 µm. The grain size of the films was found to slightly

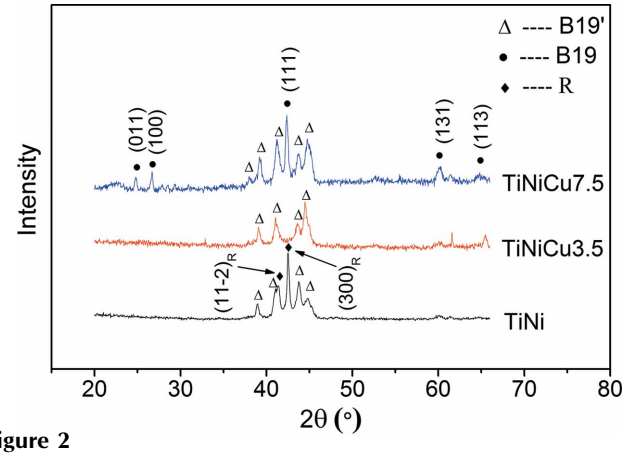

Figure 2
XRD results of the as-deposited Ti–Ni and Ti–Ni–Cu films at room temperature (X-rays, λ = 0.154 nm).

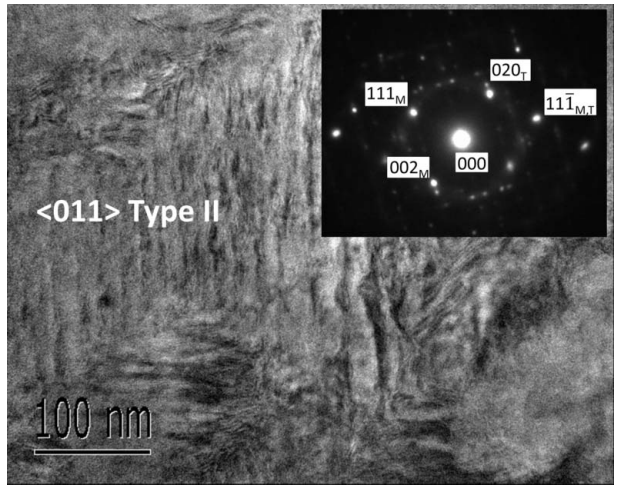

Figure 3
Bright-field micrograph of as-deposited Ti–Ni film revealing that the monoclinic martensite plates are ⟨011⟩ type-II twins. Selected area diffraction patterns with incident electron beam along $[101]_M \parallel [-110]_T$.

decrease with increasing Cu content (Ishida & Sato, 2011). However, in the Ti–Ni–Cu 7.5 as shown in Fig. 5, (011) compound twins are the dominant plates of the B19 phase; the twin widths scatter over a range from 0.02 to 0.1 µm, with the average about 0.2 µm. Instead of ⟨011⟩ type-II twins, some random B19′ martensite variants are also found.

Figs. 6(*a*)–6(*c*) show room-temperature S-XRD results of the as-obtained Ti–Ni and Ti–Ni–Cu films post-annealed at different temperatures. After post-annealing, some martensites disappear, and their diffraction peaks shift to the lower angle side with the increase of annealing temperature. For the Ti–Ni film, as shown in Fig. 6(*a*), the peaks of the R phase disappear at room temperature because the finish temperature of the martensitic transformation increases with the increase of annealing temperature. This could be explained by the formation of Ni_4Ti_3 precipitates when the annealing temperature is increased to 750°C (Miyazaki & Ishida, 1999).

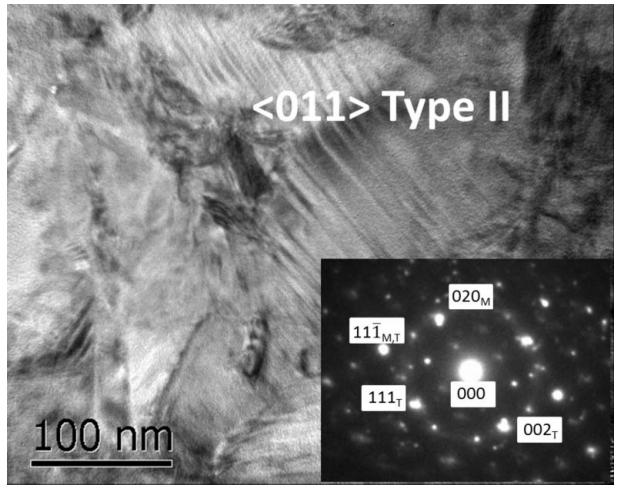

Figure 4
Bright-field TEM micrograph of as-deposited Ti–Ni–Cu 3.5 film revealing the fine ⟨011⟩ type-II twins. Selected area diffraction patterns with incident electron beam along $[101]_M \parallel [-110]_T$.

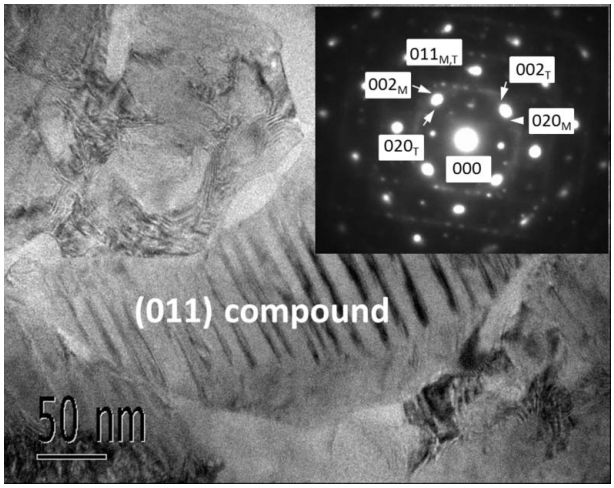

Figure 5
Bright-field micrograph of as-deposited Ti–Ni–Cu 7.5 film including the (011) compound twins. Selected area diffraction patterns with incident electron beam ∥ $[100]_{M,T}$.

However, for the Ti–Ni–Cu 3.5 film (Fig. 6*b*) and Ti–Ni–Cu 7.5 film (Fig. 6*c*), both the start and finish temperatures of the martensitic transformation decrease apparently after post-annealing, and no significant amount of precipitates were observed. With the increase of annealing temperature of the Ti–Ni–Cu films, the intensities of austenite increase. This is consistent with the previous published results from the annealed $Ti_{50.1}Ni_{40.8}Cu_{9.1}$ film (Wang *et al.*, 2012). Usually, with increasing annealing temperature of Ti–Ni–Cu films, the martensitic transformation temperature increases due to the formation of fine precipitates such as GP zones and Ti_2Cu precipitates (Ishida *et al.*, 2008). In this paper, when heating the film and substrate from room temperature to annealing temperature, a large thermal stress generated due to the different thermal expansion coefficients of the film and substrate as well as evolution of film intrinsic stress may resist the formation of fine precipitates such as GP zones and Ti_2Cu precipitates. The thermal stress can be estimated from the following equation (Fu *et al.*, 2005),

$$\sigma_{\rm th} = \frac{{\rm d}\sigma}{{\rm d}T}\,\Delta T = \left(\frac{E_{\rm f}}{1-\upsilon_{\rm f}}\right)(\alpha_{\rm Si}-\alpha_{\rm f})\Delta T, \qquad (1)$$

where α is the coefficient of thermal expansion, E is Young's modulus in austensite, ν is the Poisson ratio, the subscript 'Si' indicates the silicon substrate and that of 'f' indicates the film. We only considered the austensite for simplicity during the calculation, thus $E_{\rm f}$ was taken as 80 GPa (austenite), and $\alpha_{\rm Si}$ and $\alpha_{\rm f}$ (austenite) as $3 \times 10^{-6}\,{\rm K}^{-1}$ and $15.4 \times 10^{-6}\,{\rm K}^{-1}$, respectively, and $\nu_{\rm f}$ as 0.3 (Fu *et al.*, 2005). The calculated values of 650°C and 750°C annealed Ti–Ni–Cu 3.5 samples are 893 MPa and 1034 MPa, respectively. If the martensitic transformation occurs during cooling, these stresses will be released significantly due to the self-accommodation of martensite (Grummon *et al.*, 1999). However, it is possible that some small precipitates or defects formed during annealing, and they may have changed the intrinsic stress and cause a decrease of the transformation temperature.

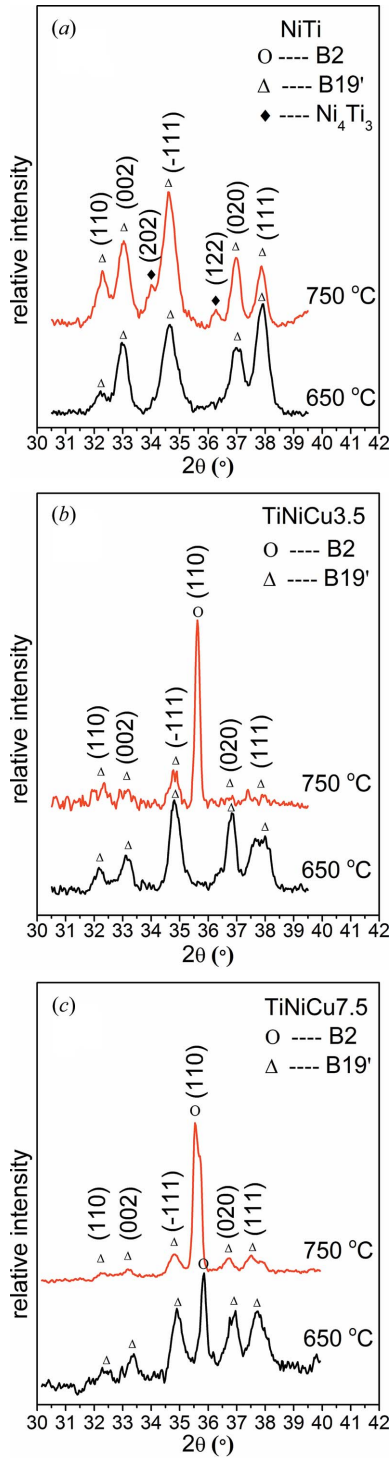

Figure 6
Room-temperature S-XRD results of Ti–Ni (*a*), Ti–Ni–Cu 3.5 (*b*) and Ti–Ni–Cu 7.5 (*c*) films post-annealed at 650°C and 750°C.

3.2. *In situ* S-XRD results of Ti–Ni film

Fig. 7 displays the *in situ* S-XRD results of the 750°C annealed Ti–Ni film. Before the tensile deformation, the dominant phase in the Ti–Ni film is B19′. During tensile loading, along the LD, the peak intensities of $(002)_{\rm B19'}$ keep increasing but those of $(020)_{\rm B19'}$ decrease. The peak intensities of $(-111)_{\rm B19'}$ and $(110)_{\rm B19'}$ decrease along the LD, and those

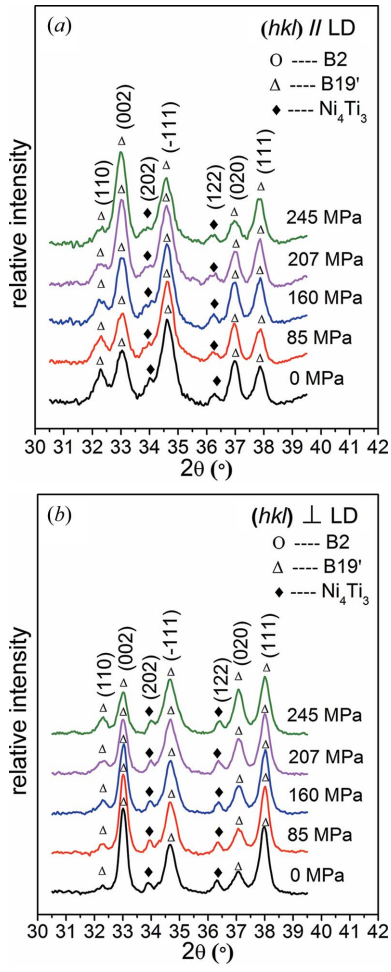

Figure 7
S-XRD results of 750°C annealed Ti–Ni film for (*a*) 0° azimuth angle and (*b*) 90° azimuth angle at different loading stages (at RT).

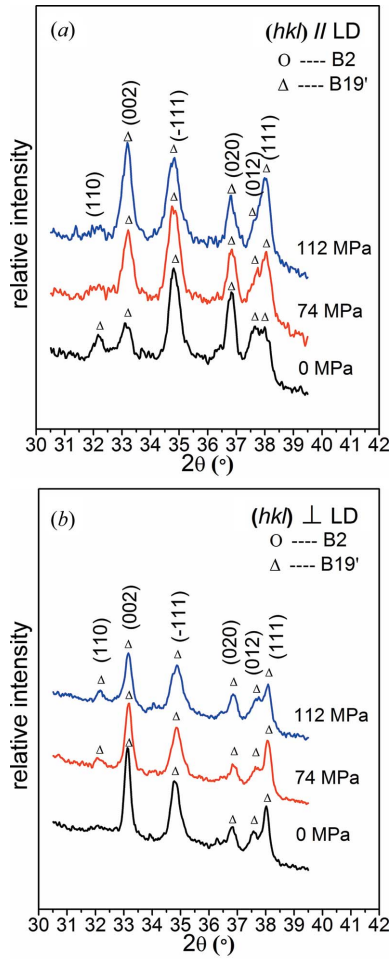

Figure 8
S-XRD results of 650°C annealed Ti–Ni–Cu3.5 film for (*a*) 0° azimuth angle and (*b*) 90° azimuth angle at different loading stages (at RT).

of the $(111)_{B19'}$ do not show significant changes. The Ni_4Ti_3 remains stable during loading. Whereas, perpendicular to the LD, all the changes in the peak intensities show reverse trends, although those of $(-111)_{B19'}$ do not show the apparent changes. The detailed re-orientation mechanisms of martensite variants during tension along two directions will be discussed in §4.

3.3. *In situ* S-XRD results of Ti–Ni–Cu3.5 film

Fig. 8 shows that, before the tensile test, martensite (B19′) is dominant for the 650°C annealed Ti–Ni–Cu3.5 film. During tensile loading, as shown in Figs. 8(*a*) and 8(*b*), the peak intensities of $(002)_{B19'} \parallel$ LD and $(020)_{B19'} \perp$ LD increase, but those of the same crystal planes decrease in the directions of $(002)_{B19'} \perp$ LD and $(020)_{B19'} \parallel$ LD. The intensities of the $(-111)_{B19'}$ and $(111)_{B19'}$ peaks do not show significant changes during the tensile process. This indicates that the orientations of certain martensite plates have been enhanced at the expense of the others, which is attributed to the detwinning or reorientation of martensite variants during uniaxial loading. Clearly, during loading, the applied stress induces changes of martensite variants and results in the preferred re-orientations of $(002)_{B19'} \parallel$ LD and $(020)_{B19'} \perp$ LD, which will be discussed in §4.

After annealing at 750°C, the Ti–Ni–Cu3.5 film shows a different room-temperature microstructure from the 650°C annealed sample, which can be revealed from the S-XRD results shown in Figs. 2 and 6. Austenite becomes dominant in the film after annealing at 750°C as shown in Fig. 9.

Similar to the report by Wang *et al.* (2012), the differences in the initial microstructures result in significant differences in the deformation behaviour of films. For the 650°C annealed Ti–Ni–Cu3.5 film, the intensities of the austenite change slightly, and the main deformation mechanism is detwinning of martensite variants. With the increase of tensile stress, the peak intensities of $(002)_{B19'} \parallel$ LD and $(020)_{B19'} \perp$ LD increase, but those of the same crystal planes decrease along their perpendicular directions. For the 750°C annealed sample, with the increase of tensile stress, the intensity of the austenite peak $(110)_{B2}$ decreases and that of the martensite peaks slightly increases. Clearly the increase rates of the martensite peaks are quite different. The peaks of $(002)_{B19'} \parallel$ LD and $(020)_{B19'} \perp$ LD increase more significantly than those of

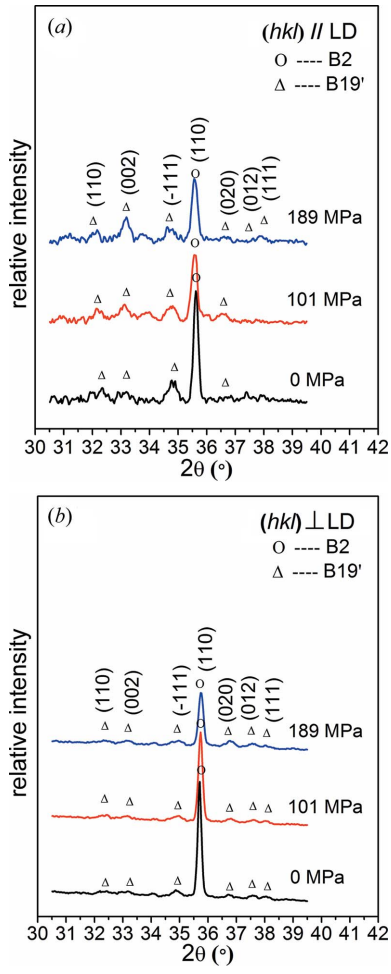

Figure 9
S-XRD results of 750°C annealed Ti–Ni–Cu3.5 film for (*a*) 0° azimuth angle and (*b*) 90° azimuth angle at different loading stages (at RT).

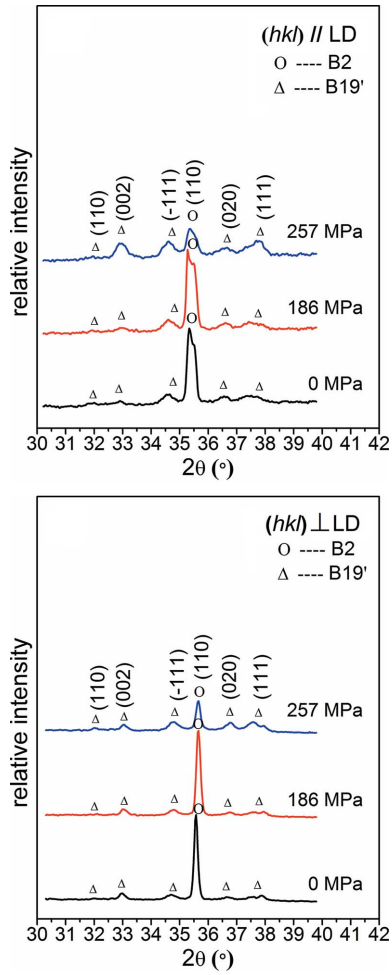

Figure 10
S-XRD results of 750°C annealed Ti–Ni–Cu7.5 film for (*a*) 0° azimuth angle and (*b*) 90° azimuth angle at different loading states (at RT).

the other oriented martensites. This clearly indicates that martensitic transformation and detwinning processes occur at the same time during deformation, and stress-induced martensitic transformation also occurs with $(002)_{B19'} \parallel$ LD and $(020)_{B19'} \perp$ LD.

3.4. *In situ* S-XRD results of Ti–Ni–Cu7.5 film

Fig. 10 shows the tensile behaviour of *in situ* S-XRD results of the Ti–Ni–Cu7.5 film annealed at 750°C. The initial microstructure is dominant by austenite, and tensile-loading-induced martensitic transformation is preferred along $(002)_{B19'} \parallel$ LD and $(020)_{B19'} \perp$ LD. Comparing the results in Fig. 10 with those in Figs. 7–9, it is concluded that the annealing temperature changes the microstructures of the Ti–Ni-based films before the deformation, and thus has a significant effect on the deformation behaviour of the films. During loading, it is found that the peak intensities of S-XRD for $(002)_{B19'} \parallel$ LD and $(020)_{B19'} \perp$ LD increase, but this is opposite to those of the same crystal planes in their perpendicular directions. This is similar to the tensile behaviour of 750°C annealed Ti–Ni–Cu3.5 film.

4. Discussion

After cooling the Ti–Ni-based films from high annealing temperatures, some twin-related neighbouring variants inside the films change their orientations to form martensitic structures in order to accommodate elastic strains applied to the martensites (Christian, 1982). In the Ti–Ni-based alloys, ⟨011⟩ type-II and (111) type-I twins were commonly observed (Otsuka & Ren, 2005), and these twinning structures were also reported to be dominant in Ti–Ni–Cu thin films with lower Cu content (less than 9%) (Miyazaki & Ishida, 1999). For the ⟨011⟩ type-II twins structure, its twin crystals are related to each other by a 180° rotational symmetry along the [0 −1 1] axis (Liu & Xie, 2003). However, for the (111) type-I twins, the twin crystals will not rotate, but are symmetrically distributed as a mirror with respect to the (111) plane. The TEM results in Figs. 3–5 clearly show the large amount of martensitic twins in the Ti–Ni-based thin films.

During the tensile loading of the above-investigated Ti–Ni-based films (see Figs. 7–10), the peaks of $(002)_{B19'} \parallel$ LD and $(020)_{B19'} \perp$ LD increase, but the same crystal planes decrease perpendicularly to the loading directions. This trend could be

well explained by reorientation of the martensitic variants (Krishnan, 1998; Ezaz & Sehitoglu, 2011), considering the existence of multiple martensitic twinning structures in these Ti–Ni–Cu thin films. For Ti–Ni and Ti–Ni–Cu3.5 films, when detwinning occurs during loading, the two twin-related variants would re-orientate and only one type of variant is left at the end of the detwinning process. Due to the rotation of the variants, the intensities of some crystal planes would decrease whereas the other planes increase, according to their orientations compared with the loading directions.

The *in situ* S-XRD results (Figs. 7–9) could explain the sequences of the detwinning process. The presence of $(020)_{B19'}$ and $(002)_{B19'}$ gives indirect evidence of the existences of ⟨011⟩ type-II twins or (111) type-I twins. Because all the above diffraction results reveal the coexistence of $(020)_{B19'}$ and $(002)_{B19'}$ planes, this clearly indicates that there are multi-variants of martensites in these annealed films. Furthermore, the interplanar angle between $(020)_{B19'}$ and $(002)_{B19'}$ is 90° in a martensitic unit-cell, the $(020)_{B19'}$ plane is obtained by rotating the $(002)_{B19'}$ plane by 180° along the $[0\text{–}11]_{B19'}$ direction as shown in Fig. 11(*a*), and the $(011)_{B19'}$ plane is the symmetrical plane of $(002)_{B19'}$ and $(020)_{B19'}$ in geometry as shown in Fig. 11(*b*). The twinning elements of the ⟨011⟩ type-II twins are as follows: twinning plane $K_1 = (0.7205, 1\text{−}1)$, shear direction $\eta_1 = [011]$, $K_2 = (011)$ and $\eta_2 = [1.5727\ 1\text{−}1]$. Thus, during the detwinning of ⟨011⟩ type-II twins, the intensities of $(002)_{B19'}$ and $(020)_{B19'}$ change inversely, but those of $(011)_{B19'}$ more or less remain at similar intensities. Although the $(011)_{B19'}$ plane could not be clearly identified from the S-XRD results, another two planes of $(-111)_{B19'}$ and $(111)_{B19'}$, which both have equal dihedral angles with the $(002)_{B19'}$ and $(020)_{B19'}$ planes, do not change apparently during the deformation of the films (Liu & Xie, 2003). This suggests that the symmetrical planes of $(002)_{B19'}$ and $(020)_{B19'}$ planes would not be significantly rotated. Therefore, we could conclude that ⟨011⟩ type-II twins exist in these Ti–Ni and Ti–Ni–Cu films, and the deformation of martensite is contributed to by the detwinning of ⟨011⟩ type-II twins. This results in the preferred orientations of $(002)_{B19'} \parallel$ LD and $(020)_{B19'} \perp$ LD. There could be other modes of twinning structures, but it is difficult to estimate the twinning mode using the S-XRD method. What we could confirm is that the occurrence of detwinning corresponds to the intensity changes of these martensitic peaks.

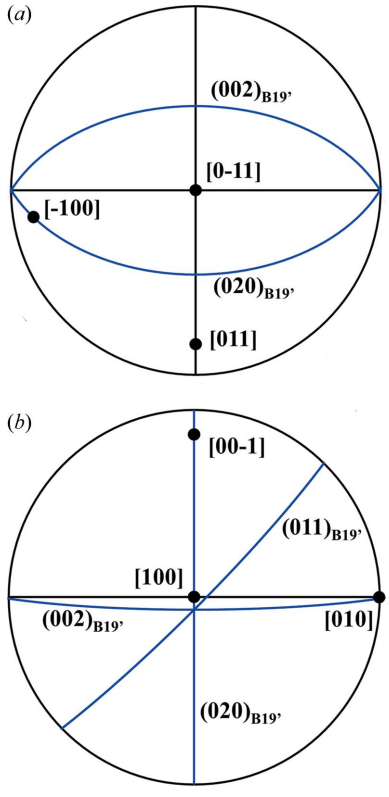

Figure 11
Stereographic projections of B19′ martensite showing the crystallographic relationship of the (002) and (020) planes: (*a*) 180° rotational symmetry about the [011] direction; (*b*) mirror symmetry about the (011) plane.

It was reported that when the Cu content is larger than 15% the Ti–Ni–Cu thin film undergoes a one-step martensitic transformation from B2 to B19 (Miyazaki & Ishida, 1999). However, when the Cu content of the Ti–Ni–Cu films is lower than 9%, the path of transformation would be B2 → B19 → B19′. When the Cu content is low and Ti is rich in the film, the transformation is only from B2 to B19′. The maximum Cu content of the films in this paper is about 7.5%. It is found that both B19 and B19′ martensite are dominant in Ti–Ni–Cu7.5. However, for the Ti–Ni–Cu films with lower Cu content, most are dominated by the B19′ martensite at the initial state, and the martensite variants are formed as ⟨011⟩ type-II twins which are often observed in Ti–Ni alloy.

5. Conclusions

Effects of film composition, microstructure and post-annealing condition on the deformation mechanisms of the Ti–Ni and Ti–Ni–Cu films were investigated using *in situ* S-XRD. The following conclusions can be obtained.

(i) With increasing annealing temperature, the growth of Ni_4Ti_3 in $Ti_{50.2}Ni_{49.6}$ film increases the transformation temperature, but the stress field of Ni_4Ti_3 could usually suppress the martensitic transformation.

(ii) For the $Ti_{50.3}Ni_{46.2}Cu_{3.5}$ and $Ti_{48.1}Ni_{40.8}Cu_{7.5}$ films, the martensitic transformation temperatures decrease with the increase of annealing temperature because of the thermal stress generated due to the different thermal expansion coefficients of the film and substrate as well as evolution of film intrinsic stress.

(iii) The deformation behaviours of the Ti–Ni or Ti–Ni–Cu films are determined by the initial state of these films. When the sample is dominated by the B19′ phase, detwinning of ⟨011⟩ type-II during tension would result in the preferred orientations of $(002)_{B19'} \parallel$ LD and $(020)_{B19'} \perp$ LD.

(iv) When annealing the films at high temperature, the B2 phase becomes dominant, and the austenite would be directly converted into martensites during loading with the same texture distributions for the situation where the B19′ phase is dominated.

The authors would like to acknowledge the grants from the National Natural Science Foundation of China (grant Nos. 11105128, 51231002, 91126001 and 51001024). YQF and XTZ acknowledge support from Carnegie Trust Funding, Royal Society of Edinburgh, Royal Academy of Engineering-Research Exchange with China and India, as well as the EPSRC Engineering Instrument Pool for providing the Differential Scanning Calorimeter (DSC, Perkin Elmer Pyris Diamond) and Hirox Digital Microscope.

References

Christian, J. (1982). *Metall. Trans. A*, **13**, 509–538.
Chu, J. P., Lai, Y. W., Lin, T. N. & Wang, S. F. (2000). *Mater. Sci. Eng. A*, **277**, 11–17.
Du, H. & Fu, Y. (2004). *Surf. Coat. Technol.* **176**, 182–187.
Ezaz, T. & Sehitoglu, H. (2011). *Appl. Phys. Lett.* **98**, 141906.
Fu, Y., Du, H., Huang, W., Zhang, S. & Hu, M. (2004). *Sens. Actuators A*, **112**, 395–408.
Fu, Y., Du, H., Zhang, S. & Gu, Y. W. (2005). *Surf. Coat. Technol.* **198**, 389–394.
Fu, Y., Huang, W., Du, H., Huang, X., Tan, J. & Gao, X. (2001). *Surf. Coat. Technol.* **145**, 107–112.
Grummon, D. S., Zhang, J. & Pence, T. J. (1999). *Mater. Sci. Eng. A*, **273–275**, 722–726.
Hammersley, A. P., Svensson, S. O., Hanfland, M., Fitch, A. N. & Hausermann, D. (1996). *High Press. Res.* **14**, 235–248.
Ishida, A. & Sato, M. (2011). *Intermetallics*, **19**, 1878–1886.
Ishida, A., Sato, M. & Gao, Z. Y. (2013). *J. Alloys Compd.* **577**, S184–S189.
Ishida, A., Sato, M. & Ogawa, K. (2008). *Mater. Sci. Eng. A*, **481–482**, 91–94.
Ishida, A., Takei, A., Sato, M. & Miyazaki, S. (1996). *Thin Solid Films*, **281–282**, 337–339.
Krishnan, M. (1998). *Acta Mater.* **46**, 1439–1457.
Kulkov, S. N., Mironov, Y. P., Danilov, V. I., Barannikova, S. A., Tolochko, B. P. & Bessergenev, A. V. (2000). *Nucl. Instrum. Methods Phys. Res. A*, **448**, 267–275.
Liu, Y. & Xie, Z. L. (2003). *Acta Mater.* **51**, 5529–5543.
Malard, B., Sittner, P., Berveiller, S. & Patoor, E. (2012). *C. R. Phys.* **13**, 280–292.
Meng, X. L., Sato, M. & Ishida, A. (2008*a*). *Acta Mater.* **56**, 3394–3402.
Meng, X. L., Sato, M. & Ishida, A. (2008*b*). *Scr. Mater.* **59**, 451–454.
Meng, X. L., Sato, M. & Ishida, A. (2009). *Acta Mater.* **57**, 1525–1535.
Meng, X. L., Sato, M. & Ishida, A. (2011). *Acta Mater.* **59**, 2535–2543.
Miyazaki, S., Fu, Y. Q. & Huang, W. M. (2009). *Thin Film Shape Memory Alloys*. Cambridge University Press.
Miyazaki, S. & Ishida, A. (1999). *Mater. Sci. Eng. A*, **273–275**, 106–133.
Otsuka, K. & Ren, X. (2005). *Prog. Mater. Sci.* **50**, 511–678.
Sun, L., Huang, W. M., Ding, Z., Zhao, Y., Wang, C. C., Purnawali, H. & Tang, C. (2012). *Mater. Des.* **33**, 577–640.
Wang, H., Sun, G. A., Chen, B., Fu, Y. Q., Wang, X. L., Zu, X. T., Shen, H. H., Liu, Y. P., Li, L. B., Pan, G. Q., Sheng, L. S. & Tian, Q. (2012). *Physica B*, **407**, 3437–3440.
Wang, Y. D., Brown, D. W., Choo, H., Liaw, P. K., Cong, D. Y., Benson, M. L. & Zuo, L. (2007). *Phys. Rev. B*, **75**, 174404.
Zarnetta, R., König, D., Zamponi, C., Aghajani, A., Frenzel, J., Eggeler, G. & Ludwig, A. (2009). *Acta Mater.* **57**, 4169–4177.
Zhang, H. J. & Qiu, C. J. (2006). *Mater. Sci. Eng. A*, **438–440**, 1106–1109.
Zhang, J. X., Sato, M. & Ishida, A. (2006). *Acta Mater.* **54**, 1185–1198.